clean technologies

MDPI

Article

Effect of Methane on Combustion of Glycerol and Methanol Blends Using a Novel Swirl Burst Injector in a Model Dual-Fuel Gas Turbine Combustor

S M Rafiul Islam [1], Ishaan Patel [1] and Lulin Jiang [1,*]

[1] Department of Mechanical Engineering, Baylor University, Waco, TX 76798, USA; smrafiul_islam1@baylor.edu; ishaan_patel1@baylor.edu

* Correspondence: lulin_jiang@baylor.edu

Abstract: Glycerol, a byproduct of biodiesel, has moderate energy but high viscosity, making clean combustion challenging. Quickly evaporating fine fuel sprays mix well with air and burn cleanly and efficiently. Unlike conventional air-blast atomizers discharging a jet core/film, a newly developed swirl burst (SB) injector generates fine sprays at the injector's immediate exit, even for high-viscosity fuels, without preheating, using a unique two-phase atomization mechanism. It thus resulted in ultra-clean combustion for glycerol/methanol (G/M) blends, with complete combustion for G/M of 50/50 ratios by heat release rate (HRR). Lower combustion efficiencies were observed for G/M 60/40 and 70/30, representing crude glycerol. Hence, this study investigates the effect of premixed methane amount from 0–3 kW, and the effect of atomizing gas to liquid mass ratio (ALR) on the dual-fuel combustion efficiency of G/M 60/40-methane in a 7-kW lab-scale swirl-stabilized gas turbine combustor to facilitate crude glycerol use. Results show that more methane and increased ALR cause varying flame lift-off height, length, and gas product temperature. Regardless, mainly lean-premixed combustion, near-zero CO and NOx emissions (≤2 ppm), and ~100% combustion efficiency are enabled for all the cases by SB atomization with the assistance of a small amount of methane.

Keywords: swirl burst (SB) injector; lean-premixed combustion; dual-fuel combustion; high viscosity; near-zero emissions

Citation: Islam, S.M.R.; Patel, I.; Jiang, L. Effect of Methane on Combustion of Glycerol and Methanol Blends Using a Novel Swirl Burst Injector in a Model Dual-Fuel Gas Turbine Combustor. *Clean Technol.* **2024**, *6*, x. https://doi.org/10.3390/xxxxx

Academic Editor(s): Name

Received: 31 August 2024
Revised: 28 September 2024
Accepted: 10 October 2024
Published: date

1. Introduction

As fossil fuel reserves continue to deplete, researchers in the field of biodiesel combustion research have turned their focus towards developing alternative sources of energy [1]. Consequently, the production of biodiesel is steadily on the rise. As biodiesel production increases, so does the generation of its byproducts. The primary and most commonly used biodiesel production process is transesterification, in which the raw material is oils and fats from plants or animals [2,3]. Biodiesel can be combusted cleanly and efficiently without preheating and further modification due to its properties similar to those of diesel. Biodiesel primarily yields glycerol ($C_3H_8O_3$) as its main byproduct [4]. The quantity of glycerol produced during biodiesel production constitutes approximately 10% of its total weight [5]. Glycerol has limited use in a few industrial sectors of cosmetics, food processing, packing material, etc. The excess glycerol production can be treated as waste, which is a challenging task to dispose of in the environment [5]. Due to the high viscosity, high surface tension, and low calorific value of glycerol, it is difficult to burn [6] with conventional injectors such as air-blast (AB) atomizers that are highly sensitive to slight variations in fuel properties. However, due to its substantial oxygen content and moderate heat output, glycerol is a feasible biofuel option for combustion, aiming to decrease carbon emissions [7,8]. On the other hand, crude glycerol from biodiesel contains

methanol [9–12], which has a high octane number, high performance, and low emissions [8,13]. Additionally, methanol can be produced from biomass [8,13]. Efficiently combusting glycerol and methanol blends can reduce the cost of purifying crude glycerol, which contains 60–70% glycerol and 23.4–37.5% methanol by weight [5]. Moreover, by blending methanol with glycerol, the viscosity of the blend reduces significantly compared to pure glycerol [8]. However, it is ~3× viscous than diesel [14], which is difficult to burn by using the AB injector [8].

In the present era, there is a worldwide inclination towards implementing strict emissions regulations to reduce global warming [8]. Scientists are actively engaged in efforts to minimize emissions through the implementation of clean and efficient combustion approaches [8]. Fine spray generation, which helps to evaporate the spray quickly and mix with air homogeneously, is a pre-requisite for clean and complete combustion [8]. However, the atomization capability of the conventional AB atomizer is limited. The AB atomizer introduces a fuel at a relatively lower velocity while injecting air at a higher velocity through the injector [8,15]. It first produces a liquid jet core or film at the injector exit, which breaks further downstream by creating long ligaments, short streaks, and large droplets gradually by shear layer instabilities between the liquid fuel and the high-velocity air [8,15–17]. When ligaments and larger droplets move further in the flow direction, aerodynamic forces by the relative velocity of the ligaments and droplets with the surrounding air break the ligaments and droplets into smaller droplets, which is called secondary atomization [8,18,19]. However, for liquid fuels with even a slight increase in viscosity and surface tension force, shear layer instabilities are suppressed, hindering the liquid disintegration to yield larger droplets and ligaments that do not fully vaporize [19,20]. Hence, they burn in diffusion mode locally, resulting in high local flame temperature and pollutant emissions [7,8,16,17,21]. For instance, sustainable aviation fuel C-3 has almost 2.5 times higher viscosity of conventional jet fuel Jet A [22,23]. Due to the limited atomization capability of AB injector while atomizing C-3, it exhibited the lowest ignition capability among the tested fuels, including Jet A-1, A-2, A-3, C-1, C-2, C-3, C-4, C-5, and C-7 [23].

Ganán-Calvo (2005) developed the flow-blurring (FB) atomizer with a significantly enhanced atomization efficiency [8,24]. Compared to the conventional AB atomizers that atomize by external air-liquid interaction, the FB atomizer uses a unique internal geometry to incur rapidly formed internal two-phase flow with entrapped air bubbles. While crossing the injector exit, the air bubbles expand and burst robustly due to the dramatic pressure drop. This tears the surrounding liquid into fine droplets immediately at the injector exit, defined as primary atomization. Hence, the FB atomizer offers a significantly larger total droplet surface area, ranging from five to fifty times greater than the AB atomizer [24]. Due to the fundamentally varied primary atomization mechanism, the FB atomizer has a broader range of fine spray generation capability irrespective of viscosity [8,16,22,25]. It generates droplets with smaller diameter and more uniform droplet size distribution. For water, the Sauter mean diameter (SMD) is 5–25 μm for FB and 5–45 μm for AB ≥2 cm downstream of the injector exit [8,21]. This creates a shorter atomization complete length (for FB ~2.67 D downstream from the injector exit with diameter of D and AB > 50D from the injector exit) [26]. FB generates fine droplets for a variety of liquids: water [26], diesel [27], biodiesel [28], vegetable oil [27], Jet A-2 [29], JP-5 [29], viscous sustainable aviation fuel C-3 [22,29], and even thin ligaments for extremely viscous glycerol at the injector immediate exit [30]. As a result, the FB injection resulted in clean, lean-premixed, and complete combustion of diesel [31], biodiesel [31], vegetable oil (VO) [31], and even straight glycerol [7] (~>200× more viscous than diesel) without preheating the fuel or the air. However, though the primary atomization generates fine droplets for distinct fuels, thin ligaments are observed for extremely viscous glycerol at the injector immediate exit [8,30]. Jiang et al. (2015) observed that larger droplets are generated at the spray periphery while atomizing water by using the FB injector [26]. Additionally, for high-viscosity glycerol, small ligaments, in addition to droplets, are

generated at the injector exit. These ligaments and larger droplets undergo a longer secondary atomization length than low-viscosity water [8,30]. This causes a long fuel pre-vaporization and fuel–air mixing zone, leading to a further-lifted-off flame that is subject to blow-off [8]. Sharma et al. (2024) investigated the effects of atomizing air to liquid mass ratio (ALR) and swirl number for preheated glycerol at 400 K and preheated air at 500 K in a swirl stabilized combustor by using the FB injector [32]. They found the lift-off height increases with the increase of ALR and swirl number [32]. FB was also utilized to combust preheated vegetable oil and glycerol at 400 K with preheated air at 500 K in a swirl stabilized combustor [33]. It was observed that with the increase in swirl number, flame stability increases [33] with cleaner combustion compared to the counter-swirl AB injector.

In order to further enhance the secondary atomization, our group recently developed a novel twin-fluid injector called a swirl burst (SB) injector by innovatively introducing swirling atomizing air (AA) with the FB concept [17,34,35]. It creates stronger shear layer interactions by forming the radial and tangential velocity components of the AA via uniquely designed swirling vane channels to disintegrate the large droplets and/or ligaments rapidly at the injector nearfield by secondary atomization [8,17,36,37]. Thus, the SB injector generates more uniform and finer droplets with diverged spray angles [8,35,37–40] than an FB injector [29,34,35]. The atomization length of the SB injector is half of the FB injector; thus, the SB yielded lower lifted-off and more compact flames of straight VO, signifying enhanced flame stability and compactness [8,34]. In addition, combustion efficiency is further improved for SB compared to FB: for non-preheated straight VO, completeness of combustion was found to be 98% by using the SB injector whereas 95% completeness was found by using the FB injector [8,17]. The SB injector achieved complete, lean-premixed combustion of straight algae oil (AO) (~16× more viscous than diesel) with ultra-low CO (6–8 ppm) and NOx (6 ppm) emissions at an equivalence ratio of 0.65 and air-to-liquid mass ratio (ALR) of 4.34, proving the fine atomization capability of the SB injector [8,36]. Furthermore, computational simulation and modeling provide insight into the fundamental two-phase atomization mechanism underlying the ultra-fine spray formation and clean combustion using the FB injection concept that shares the same primary atomization mechanism with the SB atomization. Murugan et al. (2020) found that the two-phase flow pattern of the FB injector is investigated numerically by large eddy simulation (LES) [41]. They observed that the threshold ALR for the working principle of FB injector is 0.6 [41]. Ling and Jiang (2024) investigated the internal two-phase flow dynamics and break-up mechanism of the FB atomization concept using a two-dimensional (2D) rectangular section [42]. They identified the threshold Weber number and dynamic pressure ratio at which a bubbly-jet region is generated, which is a transition regime between the AB-jet regime and the FB-jet regime formed near the liquid tube tip inside the atomizer [42]. Nasim et al. (2023) found that air penetration depth upstream of the liquid channel tip increases as the ratio of the gap between the liquid flow tube exit and atomizer exit (H) to the center liquid channel's inner diameter (D) decreases for the SB injector [43]. In addition, the numerical method utilized by Cravero et al. (2024) has the potential to establish the correlation between the injector swirl geometry and the turbulence phenomena of the two-phase atomization [44]. The recirculation length of the two-phase flow, if any, can also be numerically simulated by the 3-dimensional large eddy simulation [45].

To reduce NOx and particulate matter emissions, dual-fuel combustion is being explored in combustion systems. Papagiannakis et al. (2004) used natural gas (NG) in a dual-fuel diesel engine with the pilot diesel ignition and observed ~50–200 ppm less NOx while running at 2500 rpm and ~100–800 ppm less NOx while running at 1500 rpm compared to direct diesel combustion in a compression ignition (CI) engine [46]. By using methane (CH_4) in a dual-fuel diesel-methane combustion Guido et al. (2018) found less soot and almost a 40% reduction in particles found in the combustion gas products [47]. They also observed ~0.02–0.35 mg/L less soot concentration of dual-fuel compared to diesel combustion [46]. Moreover, in spark-ignition (SI) engines, dual-fuel combustion can

reduce emissions and enhance performance by reducing fuel consumption [48]. Iorio et al. (2013) discovered ~0.012 g/kg lower CO, ~15 g/kg lower NOx and ~2–5 g/kg less particulate emission by utilizing methane–gasoline dual fuel combustion compared to gasoline combustion in a SI engine [49]. Similarly, by utilizing biodiesel and NG dual-fuel combustion in a radial swirl gas turbine at an equivalence ratio of 0.5, found ~10 ppm less NOx compared to biodiesel combustion [50]. Chong et al. (2020) demonstrated ~1.5 g/kWh less NO at an equivalence ratio of 0.65 by using diesel-NG dual fuel combustion compared to diesel combustion in a model gas turbine combustor [51]. Additionally, using an FB injector, Jiang et al. (2014) combusted pure glycerol with methane in a 7 kw model gas turbine combustor and found that flame length becomes almost half when methane flow is increased from 4.14 slpm to 7.12 slpm with a constant heat release rate (HRR) of 7.9 kW [7,8]. Also, due to the high temperature, ~1800–2000 K, at a distance of 8 cm from the injector exit for 55% of methane by HRR, fuel pre-vaporization is faster compared to the 32% methane by HRR in glycerol and methane co-combustion at an ALR of 2.23, resulting in more homogeneous air–fuel mixing and more complete combustion with less pollutant emissions [7]. Thus, for 55% methane by HRR in the co-combustion of glycerol and methane, carbon monoxide (CO) emission is ~20 ppm and NOx emission is ~10 ppm less than the 32% methane by HRR [7].

In our previous study, by using an SB injector, we achieved ultra-low CO and NOx concentrations and promising combustion efficiency of G/M blends in the ratios of 50/50, 60/40, and 70/30, as well as at different ALRs for 50/50 ratio of G/M (1.5–3.0) [8,52]. Near-complete combustion was achieved for 50/50 with relatively lower combustion efficiency for 60/40 and 70/30 by HRR [8,52]. To further improve the combustion efficiency, the present study is concentrated on analyzing the effect of methane amount through the combustion swirler on the dual-fuel combustion performance (methane and 60/40 G/M blend by HRR) at a constant ALR of 3.0 using the SB injector for the liquid portion [8]. G/M blend of 60/40 ratio represents crude glycerol [5]. Additionally, the impact of ALRs on the G/M of 60/40 methane main flame of the dual-fuel combustion is investigated with the small quantity of premixed methane of 1 kW [8]. The equivalence ratio and total HRR are kept constant at 0.75 and 7.0 kW, respectively [8]. Flame images, concentration of CO and NOx in the combustion gas products, and combustion gas products and combustor wall temperature are also studied to determine the global combustion characteristics of the dual-fuel G/M of 60/40 methane combustion [8]. The novelty of this work mainly resides in (1) achieving lean premixed combustion with near zero NOx and CO emissions of the dual-fuel G/M 60/40-methane with the methane amount of 0–3.0 kW, without fuel nor air preheating, (2) investigating the optimum methane amount to enhance the efficiency of the duel-fuel combustion of G/M 60/40-methane blends, and (3) acquiring complete combustion of G/M 60/40-methane blends with a small amount of methane at 1 kW by using the novel SB injector at two-phase mass ratio of 2, enabling use of waste crude glycerol as a biofuel.

2. Experimental Setup

2.1. Working Principle of Swirl Burst Injector

Figure 1 illustrates the SB injector's working principle [8,17,36]. Key geometrical properties of the SB injector are provided in Table 1. Liquid fuel passes through the center channel, and atomizing air (AA) flows through the annulus around the center liquid channel [8,24]. The geometric conditions are: (i) center liquid channel inner diameter, D is equal to the exit orifice diameter; (ii) the gap between the liquid flow tube exit and atomizer exit (H) will be equal to or less than 0.25 times of the center liquid channel diameter [8,24]. While leaving the gap H, AA flows in the radial direction [8]. When the geometric conditions are achieved [12,24,36], a stagnation point develops between the center liquid fuel tube tip and the injector exit, and a small part of the AA penetrates a very short distance of the liquid fuel flow channel, which creates turbulence and forms

bubbles slightly downstream of the liquid fuel flow exit channel, resulting in significantly turbulent two-phase flow passing through the injector exit [8,24]. The air bubbles leaving the atomizer exit in the flow direction burst and break into fine droplets due to a significant pressure drop [8,17]. The remaining major portion of AA flows through the injector exit with a very high momentum which helps the secondary atomization by shear layer instabilities at the interface of the liquid parts and fast-moving air [8,36]. This process was first introduced in the FB atomization concept. In the SB injector, it innovatively integrates the advantage of the FB injection and the swirling flow to further enhance the secondary atomization. Like the FB injector, a stagnation point is developed at the same location. From the stagnation point, a small amount of air penetrates the liquid channel, and the remaining larger quantity of air moves toward the injector exit with a swirling motion through the swirl grooves and helps with the secondary atomization through shearing between the surface of droplets and swirling air [8,17,36]. The swirling flow is characterized by the injector swirl number (SN), which is a non-dimensional number determined by Equation (1) [8,53,54].

$$N = \frac{2}{3} \times \frac{1 - (d_h/d_t)^3}{1 - (d_h/d_t)^2} \times tan\,\alpha \quad (1)$$

where swirler hub diameter is denoted by d_h, tip diameter is denoted by d_t, α represents the exit vane angle of the swirler. The vane angle α is the angle between the axial plane of the curved vane and tangent to the exit of the curved vane.

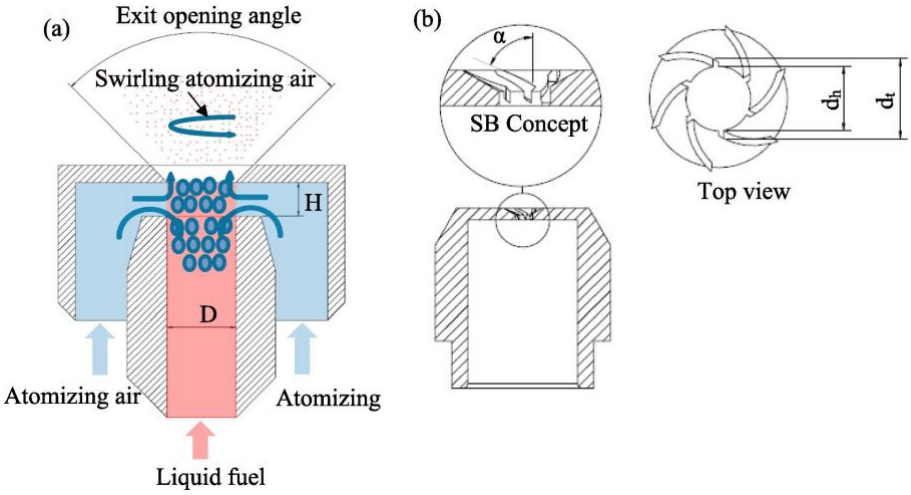

Figure 1. (**a**) Working principle of SB injector, (**b**) SB concept [8,17,36].

Table 1. Key geometrical parameters of the SB injector.

Parts	Dimensions
Center channel diameter, D	1.5 mm
The gap between the liquid flow tube exit and atomizer exit, H	0.375 mm
Hub diameter, d_h	1.5 mm
Tip diameter, d_t	2.1 mm
Exit vane angle, α	70°
Injector swirl number, ISN	2.4

2.2. Experimental Setup of the Model Dual-Fuel Gas Turbine Combustor

The objectives of the current study are to investigate (1) the effect of methane amount (0 to 3 kW by HRR) on the combustion performance of the dual-fuel (gaseous and liquid fuel) flame when methane is introduced through the combustor swirler and G/M of 60/40 (by HRR) is used as the liquid fuel blend and atomized by an SB injector at a constant ALR of 3.0; and (2) the effect of ALR on the dual-fuel G/M of 60/40-methane combustion by using the SB injector at a constant 1 kW of methane [8]. All the experiments are conducted at the constant equivalence ratio of 0.75 and the total HRR of 7.0 kW [8]. Global flame characteristics are investigated by analyzing the visual flame images, carbon monoxide (CO), and nitrogen oxide (NOx) concentrations in the combustion gas products at the combustor exit [8]. The combustion gas product temperature and the combustor outer wall temperature are measured to evaluate the combustion completeness [8].

For our current investigation, a lab-scale 7-kW swirl-stabilized gas turbine combustor was used as per Figure 2a,b [8]. To ensure dry, clean air supply to the combustor, the compressed air goes through water traps and filters, and then is divided into PA and AA [8]. The Mass Flow Controller (MFC) from Alicat MC-series controls the PA and AA supply with an uncertainty of 0.8% of the reading and ±0.2% of the full range [8]. The MFC model number for PA is MCP-250SLPM-D with a range of 0–250 SLPM, and for AA, the model number is MCP-100SLPM-D with a range of 0–100 SLPM [8]. The AA is introduced through a check valve, located at the downstream of the MFC to prevent the backflow. Before starting the experiment, methane gas is used to preheat the combustor [8]. Methane flows from the source tank and is introduced through a valve [8]. Flow was controlled by MFC of model no. MCP-50SLPM-D with a range of 0–50 SLPM [8]. Methane is mixed with PA in the mixing chamber. A ball valve is used to flow methane to the mixing chamber, while a second ball valve remains closed to prevent methane flow to the atomizer. Finally, the mixture of PA and methane passes through a 45° straight vane swirler with SN of 0.77 to the quartz combustor. It is to be mentioned that throughout the experiment, methane is premixed with the PA in the mixing chamber shown in Figure 2a and then introduced to the quartz combustor through a combustor swirler. The cylindrical quartz tube of the combustor has a length of 45 cm and a diameter of 7.62 cm [8]. Glycerol and methanol are stirred by using a magnetic stirrer with a speed of up to 3000 rpm for the mixing. The mixed fuel is introduced to the atomizer via a peristaltic pump: Cole-Parmer Masterflex L/S (EW-77921-75), Masterflex LLC, Barrington, Illinois, USA, with a range of 0–88 mLPM and an uncertainty of ±0.1% of the range, is used [8]. A pulsation damper is used between the fuel pump and the SB injector [8].

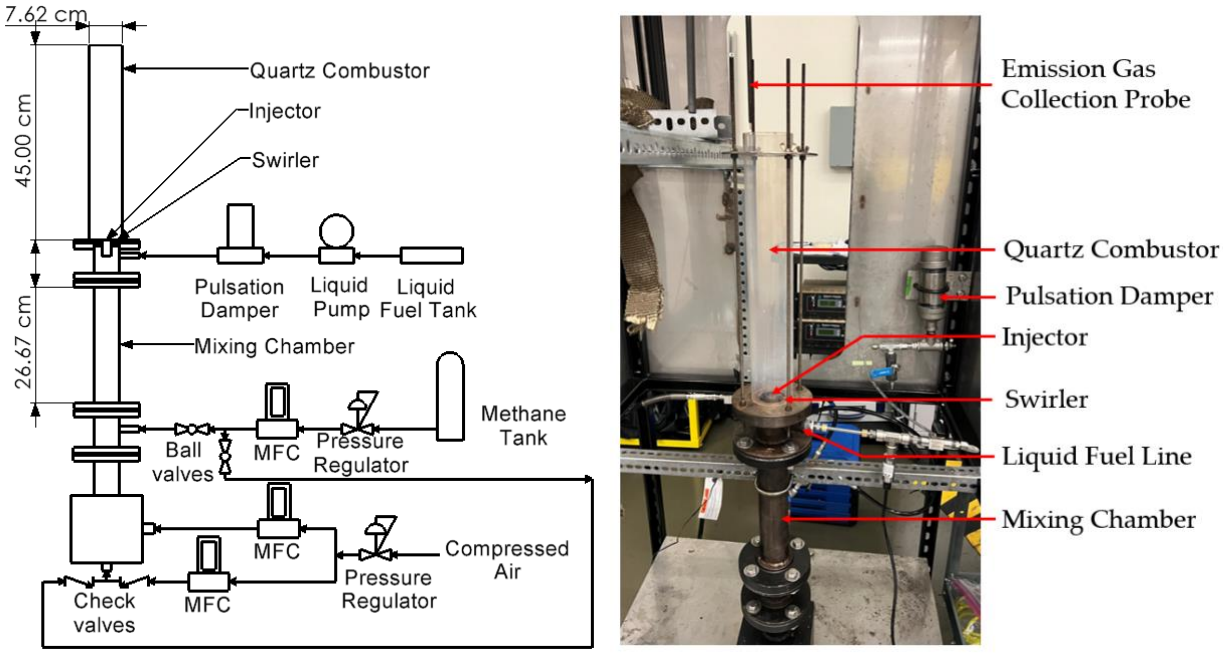

(**a**) (**b**)

Figure 2. (**a**) Schematic [8] and (**b**) the test rig of the model dual-fuel gas turbine combustor.

The research objectives of the current study are twofold: (1) it investigates the effect of premixed methane amount (0 to 3 kW by HRR) on the combustion performance of G/M of 60/40-methane dual-fuel combustion, and (2) it explores the impact of ALRs on the G/M of 60/40-methane dual-fuel combustion with 1 kW methane by using SB injector [8]. A comparison of the physical and chemical properties of pure glycerol, methanol, and G/M of 60/40 blend with diesel is provided in Table 2 [8]. Table 3 exhibits the experimental conditions for different amounts of premixed methane in the G/M of 60/40-methane dual-fuel combustion with a constant ALR of 3.0 and equivalence ratio of 0.75 [8]. Constant HRR of 7 kW and an equivalence ratio of 0.75 are maintained throughout the process for the tested cases [8]. For the effect of ALR through the liquid fuel injector on the dual fuel combustion, the AA flow rate is varied to achieve ALRs of 2.0, 2.5, and 3.0 while keeping an HRR of 7 kW and an equivalence ratio of 0.75 as constant.

Table 2. Selected physical and chemical properties of the fuels used [7,8,12,14,29,54–59].

Property	Diesel	Methanol	Glycerol	G/M of 60/40 Blend
Chemical formula	$C_{11.125}H_{19.992}$	CH_4O	$C_3H_8O_3$	N/A
Lower heating value, LHV (MJ/kg)	44.60	19.90	15.80	17.22
Density at 25 °C (kg/m^3)	834.00	791.00	1260.00	1045.46
Kinematic viscosity at 25 °C (mm^2/s)	3.88	0.59	965.80	8.02
Auto-ignition temperature (°C)	260.00	464.00	370.00	N/A
Vaporization temperature (°C)	160.00–370.00	64.70	290.00	N/A
Heat of vaporization (kJ/kg)	250.00	726.10	662.00	N/A
Stoichiometric air/fuel ratio (mol/mol)	16.12	7.14	16.66	10.92

Table 3. Experimental conditions for G/M of 60/40-methane dual-fuel combustion at ALR of 3.0.

ALR	HRR of G/M of 60/40 Fuel	HRR of Methane (kW)	G/M of 60/40 Blend Volume Flow Rate (MLPM)	Methane Flow Rate (SLPM)	Atomizing Air Flow Rate (SLPM)	Primary Air Flow Rate (SLPM)

	(kW)					
3.0	7.0	0	23.33	0	57.37	86.99
3.0	6.8	0.2	22.67	0.33	55.74	88.05
3.0	6.6	0.4	22.00	0.67	54.10	89.12
3.0	6.4	0.6	21.33	1.00	52.46	90.18
3.0	6.2	0.8	20.67	1.33	50.82	91.25
3.0	6.0	1.0	20.00	1.67	49.18	92.33
3.0	5.5	1.5	18.33	2.50	45.08	94.97
3.0	5.0	2.0	16.67	3.34	40.98	97.64
3.0	4.5	2.5	15.00	4.17	36.88	100.30
3.0	4.0	3.0	13.33	5.00	32.79	102.96
2.5	6.0	1.0	20.00	1.67	40.98	100.51
2.0	6.0	1.0	20.00	1.67	32.79	108.70

To analyze global combustion characteristics, CO and nitrogen oxides (NOx) concentrations in the combustion gas products are measured by an ENERAC (700 series) emission gas analyzer. For NOx detection, the range is 0–150 ppm and 0–1500 ppm (dual mode) with a resolution of 0.1 ppm and an uncertainty of <±1% of the reading. CO is measured by a four-electrode electrochemical sensor with a range of 0–150 ppm and 0–2000 ppm (dual mode), the resolution of 0.1 ppm, and the uncertainty of ±1–2% of the reading [8]. The flame images are meticulously captured by using a Canon EOS M50 Mark II, Canon U.S.A. Inc., Huntington, NY, USA, with an aperture setting f/4.5, light sensitivity settings of International Organization for Standardization (ISO)-6400 (ISO)-6400 [60], an exposure time of 1/125 s, and a focal length of 17 mm [8]. A R-type thermocouple with a range of -50–1480 °C and uncertainty of ±1.5 °C or ±0.25% of the reading is used to measure the combustion products gas temperature at 2.54 cm upstream of the combustor exit in the radial direction of the quartz combustor tube [8]. To measure the surface temperature of the quartz combustor tube, a LS-84D thermometer with a J-type thermocouple (Omega HPS-HT-J-12-SMP-M) with a range of 0–760 °C and uncertainty of (±0.5% of reading + 0.7 °C) is used [8]. The temperature of the combustion products gas is measured at the combustor exit (2.54 cm upstream the opening) at nine equidistant radial locations. Combustor wall temperature is measured at nine equidistant axial locations. Both temperatures are continuously monitored. At each measured location, the temperature stabilizes after several minutes within a fluctuating range with ~6–8 K variation from the lowest to the peak value. To minimize thermocouple error, the average of the upper and lower bounds of the fluctuating temperature data is recorded.

3. Results and Discussion

3.1. The Effect of Methane Amount in the Dual-Fuel Combustion

3.1.1. Global Flame Characteristics for Various Methane Amount in the Dual-Fuel Combustion

The Effect of Methane Amount on Visual Flame Images

In this study, the effect of methane amount on global combustion characteristics of the dual-fuel flames is analyzed in terms of visual flame image, thermal characteristics and CO, and NOx concentrations of the combustion gas products. Properties of 60/40 G/M are illustrated in Table 2 [8]. The kinematic viscosity of 60/40 G/M is ~2× that of diesel fuel, making it difficult to be finely atomized using a conventional AB injector due to the AB injector's sensitivity to small change in fuel properties [8]. Instead, the current work employs the SB injection that has demonstrated high viscosity tolerance as aforementioned [8]. Figure 3 shows the flame images of 60/40 G/M and 60/40 G/M methane dual-fuel with the varying methane amount of 0.2 kW to 3.0 kW, where total HRR is maintained at 7 kW with ALR of 3.0 and equivalence ratio of 0.75 [8]. Each visual

flame image is captured at an exposure time of 0.008 s, which significantly exceeds the chemical time scales of elementary reactions, e.g., at the order of magnitude of ~10^{-4}s for OH* [61]. Hence, each flame image is an ensemble flame image of a time averaging process of fast-changing chemical kinetics and varying flame stages within the exposure time. The ensemble flame images thus illustrate average flame lift-off height and flame length. The image brightness is increased by 50% to analyze the flame qualitatively [8]. Blue chemiluminescence of the flames reflects complete combustion of CH* [35,61]. Therefore, in all cases, the predominant blue flames suggest that the complete and clean combustion is achieved for the high-viscosity pure-liquid 60/40 G/M fuel blend and the dual-fuel combustion of G/M of 60/40 and methane by using a powerful SB injector even without fuel or air pre-heating and with an uninsulated combustor [8]. It is to be noted that the red color on the quartz combustor is the result of the reflection of the flame zone on the quartz combustor wall. Fuel pre-vaporization and fuel–air mixing likely occurs in the dark region upstream of the flame which signifies mainly lean-premixed combustion attained by the ultra-fine SB atomization [8]. The highly illuminated portion at the middle of the flame illustrates the high-temperature primary reaction zone [8]. It is observed that the lift-off height of the pure-liquid G/M of 60/40 fuel is ~10 cm, for G/M of 60/40 methane dual-fuel at 0.2 kW methane is ~8 cm, which decreases gradually with the increase in the amount of the methane and becomes ~5 cm for the flame with 3 kW premixed methane [8]. Flame length also becomes shorter with the increment of methane amount with more radially distributed flame: pure-liquid G/M of 60/40 fuel flame length is ~12 cm (y = ~10–22 cm); for G/M of 60/40-methane dual-fuel at 0.2 kW methane, flame length is ~11 cm (y = ~8–19 cm); and at 3 kW, methane length is ~8 cm (y = ~5–13 cm) [8]. The possible reasons mainly contributing to these trends are: (1) the addition of highly reactive methane enhances the reaction rates resulting in less lift-off height with a shorter flame length; (2) thus the local flame temperature is also increased in return, vaporizing the liquid droplets faster by quickly providing more thermal feedback that expedites complete pre-vaporization of droplets; (3) the rapidly vaporized liquid fuel mixes with oxidizer quickly and more homogeneously, thus leading to rapid reactions with a higher flame temperature in return; and (4) to keep the HRR constant, with the increase in methane, liquid fuel flow rate, and AA flow rate decrease for the constant ALR of 3.0 [8]. Hence, the injection velocity decreases, causing less lift-off height [62,63]. Thus, the flame is stabilized closer to the combustor swirl with more residence time for complete combustion [8]. Note that high-fidelity measurements of the flow-turbulence-chemistry interaction in the combustion field are needed to further validate these possible reasons, which is beyond the scope of the current global flame characterization. The flames are not radially symmetric, possibly due to the turbulent nature of the flame and/or imperfections in the manufacturing of the combustion swirler vanes, leading to uneven primary air flow.

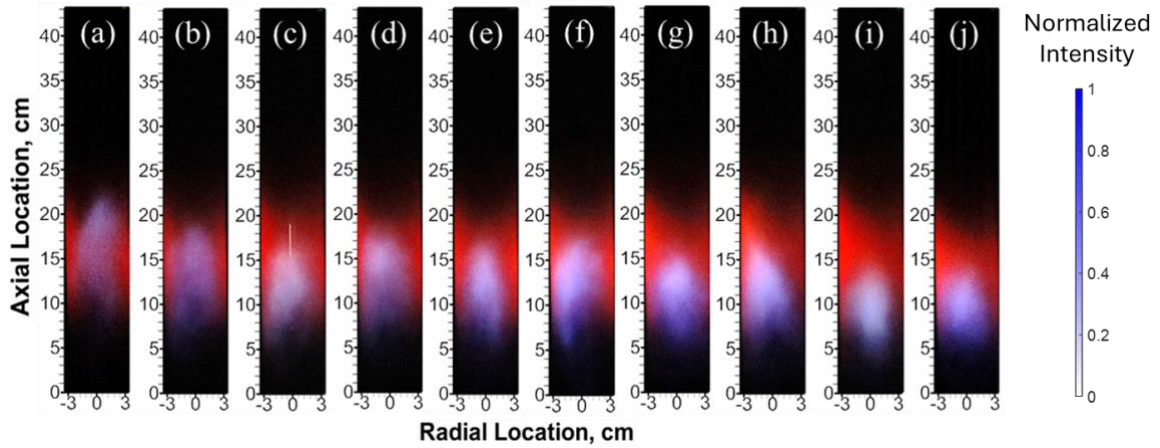

Figure 3. Flame images for (**a**) pure-liquid G/M of 60/40, and dual-fuel combustion of G/M of 60/40-methane with the methane quantity of (**b**) 0.2, (**c**) 0.4, (**d**) 0.6, (**e**) 0.8, (**f**) 1.0, (**g**) 1.5, (**h**) 2.0, (**i**) 2.5, and (**j**) 3.0 kW at a constant ER of 0.75, ALR of 3 and total HRR of 7 kW using the SB injector [8].

Figure 4 exhibits the quartz glass outer wall uncorrected surface temperature [8]. From Figure 3, it is observed that the most illuminating zone, representing the primary reaction zone is at the middle of the flame which is consistently substantiated by the quartz glass outer wall temperature profile [8]. Temperature increases from the dump plane up to the middle of the quartz combustor and then decreases in the downstream direction of the combustor [8]. It is also observed that the location of the highest wall temperature shifts in the downstream direction with the decrease of methane amount in the combustor supporting the increased lift-off height and shorter flame length with the decrease in methane amount, as per Figure 3 [8].

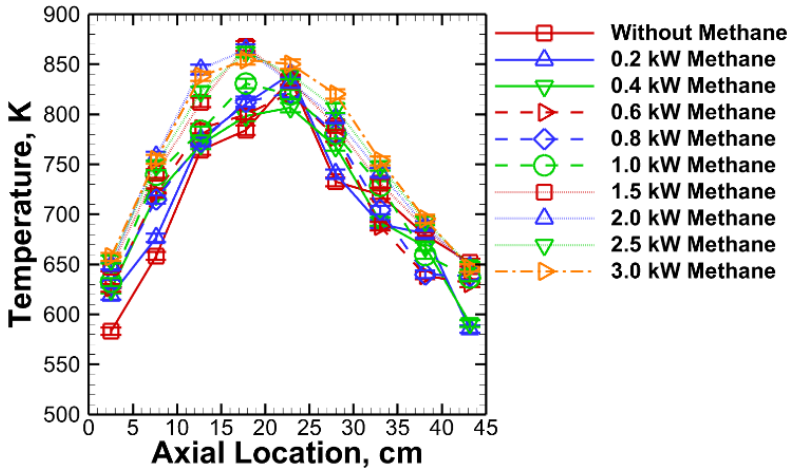

Figure 4. Axial profile of combustor outer wall surface temperature of pure-liquid G/M mix of 60/40 and G/M of 60/40-methane dual fuel combustion at a constant ER of 0.75, ALR of 3 [8].

The Effect of Methane Amount on Emissions in Combustion Gas Products

Figure 5a presents the radial temperature profile (uncorrected) of the combustion gas products at the combustor exit [8]. For all cases, temperature profiles follow a similar trend with lower temperature in the near wall zone compared to the middle of the combustor due to the convection and radiation heat loss of the uninsulated combustor wall to the surrounding [8]. The temperature profiles are not perfectly symmetric on both sides of the combustor, possibly due to the unevenly distributed primary air through the imperfectly manufactured combustion swirl and/or the turbulent nature of the flame. Temperature increases slightly with the increase in premixed methane mainly due to the high reactivity and flame speed of the methane [8]. This trend can also be substantiated by the estimated adiabatic flame temperature in Figure 6, which is 1887.7 K without methane, whereas with 3.0 kW methane, it increases up to 1909.6 K [8]. Though the difference in estimated adiabatic flame temperature from the case without methane to the dual-fuel flame with 3 kW methane is 21.9 K, the difference in gas product temperature at the combustor exit is higher than 21.9 K. This can be likely attributed to (1) the different volumes and length of the flame without methane and those with varying amounts of methane, as in Figure 3, at the constant total HRR of 7 kW, resulting in various local flame temperature, gas product temperature, and combustor wall temperature; (2) various amounts of heat loss from the uninsulated combustor to the surroundings through convective and radiative heat transfer. Figure 5b shows the CO emissions are ≤2 ppm irrespective of the methane amount in the combustor for all the tested cases [8]. Figure 5c illustrates NOx

concentration in the combustion products. Estimated adiabatic flame temperature from without methane to 3 kW methane in the dual-fuel combustion of glycerol/methanol–methane is 1887.7 K to 1909.6 K. Additionally, the uninsulated combustor wall temperature ranges approximately between 750 K to 900 K for all the cases in the reaction zone, where the flame temperature and the combustor wall temperature peak shown in Figure 4. Hence, there is considerable heat loss through the quartz combustor wall to the ambient air by radiation and convection. As a result, the flame temperature is significantly lower than 1800 K, above which thermal NOx forms [61]. Note that there might be minimal thermal NOx, less than the resolution (0.1 ppm) of the NOx measurement capacity of the emission gas analyzer. Therefore, the thermal NOx is ~0 in the current study without fuel nitrogen. Thus, the near-zero concentrations of CO and NOx suggest nearly complete and thus clean combustion achieved for the highly viscous G/M blends with/without methane. This can be again explained by the fact that the SB injector generates very fine droplets, leading to fast pre-evaporation and thus subsequently mainly lean-premixed and complete combustion [8,40]. CO_2 concentration in the gas products at the combustor exit is illustrated in Figure 5d. From pure-liquid G/M of 60/40 fuel to G/M of 60/40 methane dual-fuel combustion, the radial profiles of CO_2 emissions almost overlap. CO_2 increases with an increase in premixed methane up to 2 kW, then reduces slightly at higher methane flows. This is likely due to the increment of highly reactive methane; more O_2 participates in the reaction, generating more CO_2 in the exhaust gas, with an increment in combustion completeness. Note that the CO_2 profiles qualitatively represent the trend and may not the exact values as the sensor of the emission analyzer detects and measures CO, NOx, and O_2 but calculates CO_2 using the O_2 values and the internal algorithm based on preset fuels that are not the current fuel blend.

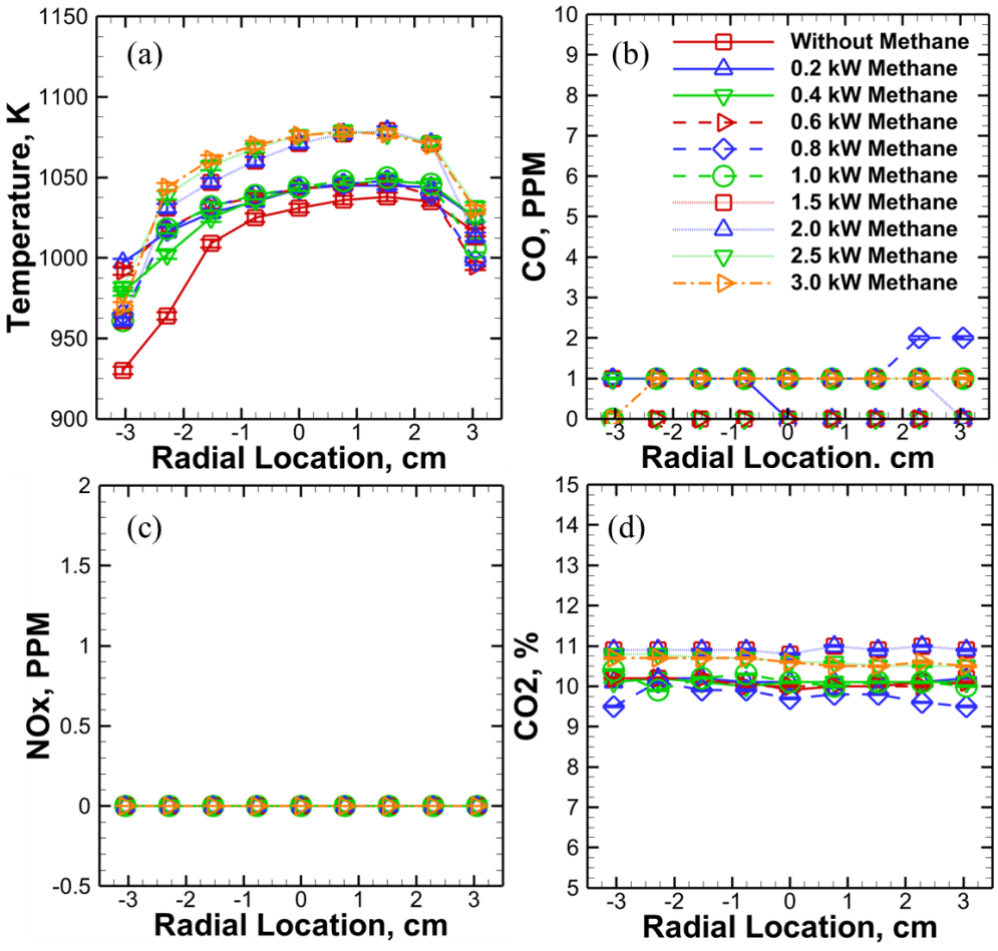

Figure 5. Radial profiles of (**a**) combustion product temperature [8] and (**b**) CO [8], (**c**) NOx, and (**d**) CO_2 concentrations at the combustor exit of pure-liquid G/M mix of 60/40 and G/M of 60/40 methane dual fuel combustion at a constant total HRR of 7 kW, ER of 0.75, and ALR of 3 using the SB injector.

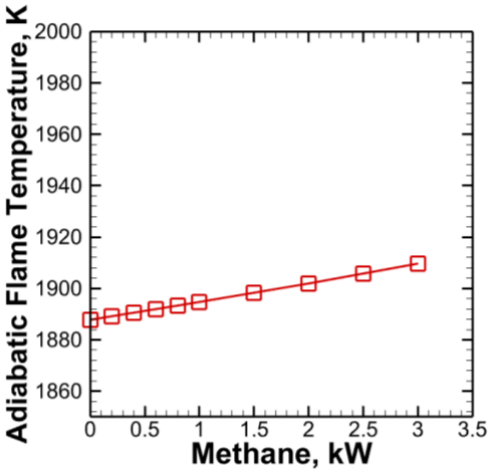

Figure 6. Adiabatic flame temperature of pure-liquid G/M blend of 60/40 and G/M of 60/40 methane dual fuel combustion at a constant ER of 0.75, ALR of 3 [8].

3.1.2. Combustion Completeness Estimation for the Varying Methane Amount

The temperature of the combustion gas products is measured by an R-type thermocouple, which is prone to error due to significant heat loss by the bead to the surrounding through radiation mostly [8,64]. To minimize the error of the thermocouple, corrected gas temperature is estimated by using Equation (2) [8,64].

$$h_t(T_g - T_t) = \varepsilon_b \sigma (T_t^4 - T_s^4) \quad (2)$$

where T_g is true gas temperature; T_t is thermocouple reading; T_s is ambient temperature, which is 22.2 °C, ε_b is the emissivity of the thermocouple bead, which is a function of combustion gas product temperature and thermocouple bead materials. It is estimated based on the correlation of R-type thermocouple and combustion gas products temperature, as per the referenced studies [65–67]; estimated values of the thermocouple bead emissivity are 0.136, 0.139, 0.138, 0.138, 0.138, 0.139, 0.141, 0.141, 0.142, and 0.142 without methane and 0.2 kW, 0.4 kW, 0.6 kW, 0.8 kW, 1.0 kW, 1.5 kW, 2.0 kW, 2.5 kW, and 3.0 kW with methane, respectively [65–67]. σ is the Stefan–Boltzmann constant, and forced convective heat transfer coefficient h_t of the combustion gas product flow is approximated using air properties [64]. The estimated values of h_t are 29.249 W/m²K, 29.828 W/m²K, 29.6989 W/m²K, 29.456 W/m²K, 29.329 W/m²K, 29.314 W/m²K, 29.420 W/m²K, 29.348 W/m²K, 29.265 W/m²K, and 29.076 W/m²K without methane and 0.2 kW, 0.4 kW, 0.6 kW, 0.8 kW, 1.0 kW, 1.5 kW, 2.0 kW, 2.5 kW, and 3.0 kW with methane, respectively [64].

Total energy released by the combustion is equal to the energy carried away by the combustion gas and heat loss to the surroundings by the combustor wall, as per Equations (3)–(5) [8,17].

$$Q_{total} = Q_{gas} + Q_{losses} \quad (3)$$

$$Q_{gas} = m_g C_{P_{air}} T_g \quad (4)$$

$$Q_{losses} = h_a A_s (T_w - T_{surr}) + \varepsilon_{glass} \sigma A_s (T_w^4 - T_{surr}^4) \quad (5)$$

where, Q_{total} is the total energy released from the combustion process; Q_{gas} is the energy carried away by the combustion gases; Q_{losses} are the energy losses by convection and radiation heat transfer from the combustion gases through the combustor outer wall to

the surroundings; m_g is the mass flow rate of the combustion gases which is equal to the total mass of fuel and gas; $C_{P_{air}}$ is the isobaric specific heat capacity of the combustion gases at the combustion gas temperature, T_g; air properties are used for the combustion products in this simple estimate. The estimated values of $C_{P_{air}}$ are 1.255 kJ/kgK, 1.262 kJ/kgK, 1.261 kJ/kgK, 1.260 kJ/kgK, 1.259 kJ/kgK, 1.259 kJ/kgK, 1.265 kJ/kgK, 1.265 kJ/kgK, 1.265 kJ/kgK, and 1.263 kJ/kgK without methane and 0.2 kW, 0.4 kW, 0.6 kW, 0.8 kW, 1.0 kW, 1.5 kW, 2.0 kW, 2.5 kW, and 3.0 kW with methane, respectively [64]; T_w is the combustor outer wall surface temperature of corresponding surface area A_s; σ is the Stefan–Boltzmann's constant; T_{surr} is the surrounding or ambient temperature, which is 22.2 °C, the ambient temperature of the laboratory environment where experiment is conducted; ε_{glass} is the emissivity of quartz glass that is a function of combustor wall temperature T_w and quartz glass average thickness of 2.136 mm [68]; for the wall temperature in 9 axial locations as illustrated in Figure 4, for each case from 0 kW methane to 3 kW methane, 9 estimated emissivity data points are obtained by using Ref. [68]; h_a is the natural convective heat transfer coefficient of the surrounding air for the heat loss from the combustor wall to the ambient air [69] and is a function of temperature; again, for the wall temperature in 9 axial locations as illustrated in Figure 4, for each case from without methane to 3 kW methane, 9 estimated the natural convective heat transfer coefficient data points are obtained by using Ref. [69].

Irrespective of the methane amount in the dual-fuel combustion, this simple estimation indicates a combustion completeness of ~100% compared to the lower efficiency of pure-liquid fuel combustion of G/M 60/40 [14]. It is to be mentioned that air properties were used for the combustion products in this simple estimate. Due to the above assumptions made, this estimation serves as a qualitative indicator rather than an absolute measure. In addition, the asymmetry of the flame in the radial direction might affect the combustor product gas temperature at the combustor exit and the combustor wall temperature measurement, thus the estimation of combustion completeness. The actual degree of combustion completeness may vary slightly. Regardless of this simple estimate, the measured combustion exhaust temperature and concentration, as well as the blue flame chemiluminescence for complete combustion of CH* [36,61], combinedly suggest the ~100% complete combustion achieved in the current study. In addition, our previous study showed that owing to the fine atomization capability of FB injector, sharing the same primary atomization by bubble bursting with the SB injection, highly viscous pure glycerol (~250 times more viscous than diesel) was atomized finely [30] and a relatively low CO (<40 ppm) was achieved in an insulated lab scale 7-kW combustor while co-combusting 68% or 45% of pure glycerol by HRR with the remaining HRR from methane at the ALR of 2.23 [7]. With further advanced atomization capability of the SB injector, clean, lean premixed (LPM), and near-complete combustion was achieved for straight algae oil and vegetable oil which are more viscous than 60/40 G/M blend [17,36]. In our present study, it is observed that ~100% combustion completeness is achieved by introducing premixed methane through the combustor swirler. This is due to the high reactivity and adiabatic flame temperature of methane [61] that helps to fully vaporize the droplets in addition to the fine atomization capability of the powerful SB injector.

3.2. The Effect of ALR

3.2.1. Global Flame Characteristics for Various ALRs of G/M of 60/40 Methane Dual-Fuel Combustion

The Effect of ALR on Visual Flame Images

Prior studies showed that an increase in ALR leads to finer atomization with very low CO emissions, ≤4 ppm, for ALR values of 3.0 for 50/50 G/M ratio fuel combustion [8,14]. In this study, the effect of ALR is observed for high-viscosity G/M of 60/40 blend with methane (1 kW) dual-fuel combustion by using a novel SB injector at a constant total HRR of 7 kW and an equivalence ratio of 0.75 [8]. For all the ALRs, the main blue flame

indicates clean combustion [35] of high-viscosity 60/40 G/M blend [8]. In the dark region upstream of the flame, pre-vaporization and fuel-air mixing occurs, which indicates the achievement of lean premixed combustion [8]. Thus, the SB injector finely atomizes high-viscosity fuel without pre-heating [8]. It is observed that an increase in ALR results in a shorter flame length [8] and a slightly shorter flame lift-off height. Figure 7 shows that for ALR of 2.0, flame length is ~16 cm (y = ~7–23 cm), at ALR of 2.5, it becomes ~15 cm (y = ~5–20 cm), and for ALR of 3.0 it becomes 11 cm (y = ~5–16 cm) [8]. The probable main reasons behind this trend are: (1) for the low ALRs, droplets are slightly bigger than those at a higher ALR and may travel further downstream along the combustor due to a higher momentum, leading to a longer flame length; (2) at the higher ALR, droplets become smaller, evaporate faster, and combust with a shorter residence time resulting in a less lifted and more compact flame [8]. Figure 8 depicts the uninsulated quartz combustor outer wall temperature (uncorrected) [8]. Quartz combustor outer wall temperature increases to the peaks and then decreases along the axial direction. Note that the flames are radially asymmetric as per Figure 7, which may result in an increased uncertainty of the combustor outer wall temperature.

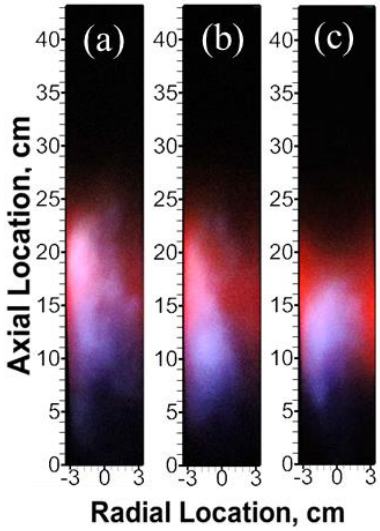

Figure 7. Flame images for dual-fuel combustion of G/M (60/40)-methane (1 kW) at ALRs of (**a**) 2.0 (**b**) 2.5 and (**c**) 3.0 at a constant HRR of 7 kW and the equivalence ratio of 0.75 [8].

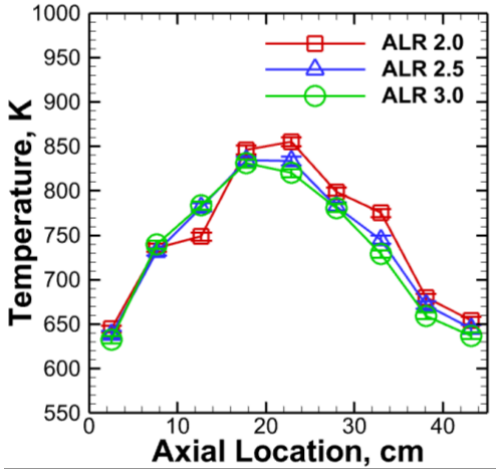

Figure 8. Axial profile of combustor outer wall surface temperature of dual-fuel combustion of G/M (60/40) methane (1 kW) for various ALRs across the SB injector at a constant ER of 0.75 [8].

The Effect of ALR on Emissions in Combustion Gas Products

Figure 9a shows that a slight decrease in ALR results in higher temperature compared to higher ALRs [8]. This might be due to (1) some of the slightly larger droplets at ALR of 2.0 burn at diffusion combustion mode without complete vaporization, resulting in slightly higher local temperature and thus higher local CO and NOx concentrations, as in Figure 9b,c compared to ALR of 2.5 and 3.0; (2) for the lower ALR of 2.0, the lower AA at the constant liquid flow rate compared to that of ALRs of 2.5 and 3.0 results in a lower injection velocity, i.e., the droplet velocity [8]. This allows a longer residence time of the droplets in the combustor, though they might be relatively larger [8]. Thus, the fuel may burn more completely with higher heat released, leading to higher combustion product temperatures [8]. For all the ALRs the CO concentrations are less than 3 ppm and NOx < 2 ppm which are illustrated in Figure 9b and Figure 9c respectively. The ultra-low CO and NOx emissions are achieved for a high-viscosity 60/40 G/M blend by using the novel SB injector, indicating near complete combustion [8]. Additionally, CO emission is uniform throughout the radial direction of the combustor exit again suggesting the generation of very fine and/or uniform droplet size by the SB injector [8]. For the ALR of 2.0, the combustion gas product temperature is slightly higher compared to the ALRs of 2.5 and 3.0, which possibly led to a slight increase in NOx at ALR of 2.0.

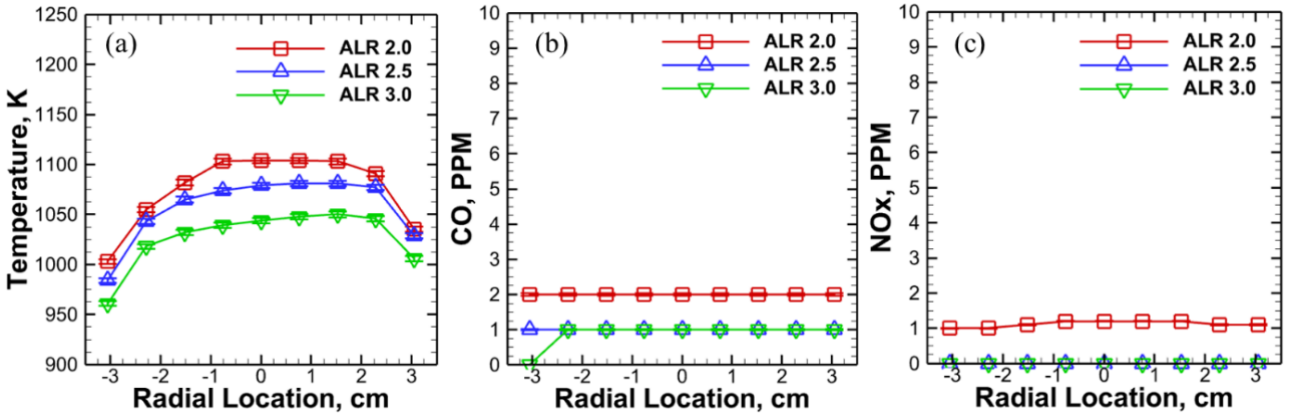

Figure 9. Radial profiles of (**a**) combustion product temperature and concentrations of (**b**) CO and (**c**) NOx at the combustor exit of dual-fuel combustion of G/M (60/40) methane (1 kW) for various ALRs across the SB injector at a constant ER of 0.75 and a constant total air flow [8].

From Figure 10a, it is evident that carbon dioxide concentration is higher for an ALR of 2.0 compared to ALRs of 2.5–3.0. This trend signifies more complete combustion at an ALR of 2.0. This may be because at the lower ALR, the injection velocity is lower, which leads to more residence time for the fuel to combust completely. Figure 10b represents oxygen concentrations in the gas products at the combustor exit. Oxygen composition is lower for an ALR of 2.0 compared to other ALRs, showing an adverse trend compared to the CO_2 profiles as expected. More oxygen consumption generates more complete combustion with increased CO_2 in the product, with less remaining oxygen in the combustion gas products.

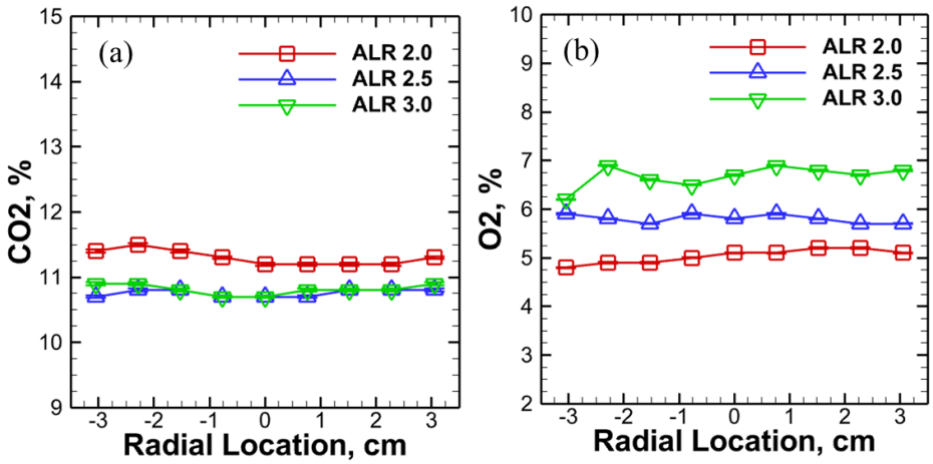

Figure 10. Radial profiles of (**a**) CO_2 and (**b**) O_2 emissions at the combustor exit of dual-fuel combustion of G/M (60/40)-methane (1 kW) for various ALRs across the SB injector at a constant ER of 0.75 and a constant total air flow.

3.2.2. Combustion Completeness Estimation for the Varying ALRs

The total generated heat is estimated by adding the heat loss to the surroundings through an uninsulated quartz combustor by radiation and convection with the energy carried away by the combustion gas products [8,17,70]. Thermocouple error is minimized by considering thermocouple bead heat loss to the surroundings through radiation as per Equation (2) [8,17]. Total energy produced is estimated by using Equations (3)–(5) [8,17]. The specific heat capacity of the combustion gases $C_{P_{air}}$ is estimated at the true gas temperature, T_g [8]. For the ALRs of 2.0, 2.5 and 3.0, the simple combustion completeness estimation results in ~100%. Again, this estimation provides qualitative information due to the assumptions made. However, again in combination of the simple estimation and the very low CO and NOx emissions as per Figure 9b,c, it can be concluded that due to a very fine atomization capability of the SB injector, at ALRs of 2.5 to 3.0, more complete combustion is achieved.

4. Conclusions

In the present study, glycerol/methanol (G/M) blends, representing waste crude glycerol from biodiesel production, are co-combusted with methane to achieve clean and complete combustion, compared to the baseline case of pure-liquid G/M combustion. This simultaneously allows us to explore renewable energy and minimize the burden of waste management. The novel SB injector is utilized to finely atomize the highly viscous G/M 60/40 blend for clean combustion without fuel preheating. Methane is added due to its high reactivity and high energy density to facilitate thermal feedback to vaporize the fine droplets quickly and combust cleanly [8], further overcoming the high evaporation and auto-ignition temperature of the glycerol component. In this study, the SB injector achieved ultra-clean combustion with CO concentration ≤ 2 ppm and ~0 ppm NOx concentration without preheating the viscous G/M and the dual-fuel burner, irrespective of methane amount from 0–3.0 kW at the total HRR of 7.0 kW. The visual flame images indicate that the increase in premixed methane via the combustion swirler results in shortened flame lift-off height and flame length with increased gas product temperature. Less lifted and more compact flames are obtained with the increase in ALR from 2.0 to 3.0. Near-zero CO and NOx concentrations are obtained for the ALRs of 2.0, 2.5, and 3.0 with a small amount of methane (1 kW), indicating the fine atomization capability of the SB injector. In addition, the simple estimate of combustion completeness, CO and NOx concentrations, and the blue flames combinedly suggest that with 1 kW of methane, at the ALRs of 2.5 and 3.0, almost-complete combustion is achieved for the main flame of

glycerol/methanol blend 60/40. Hence, the optimum ALR is 2.5 for the current experimental setup and conditions since an ALR of 2.5 has lower atomizing air flow compared to that at an ALR of 3.0. This requires less energy input for complete combustion. In summary, the dual-fuel combustor with the novel SB injector achieved lean-premixed, complete or near complete combustion of a highly viscous glycerol/methanol blend of 60/40 with/without methane and without fuel or air preheating in an uninsulated combustor. Thus, the novel SB injector coupled with/without co-combustion of a small amount of premixed methane potentially enables direct use of the crude glycerol for ultra-clean energy generation from the biofuel production waste, eliminating the expenditure of post-processing of waste crude glycerol [8]. The primary advantages and limitations of the current study are summarized in Table 4.

Table 4. Advantages and limitations of the current study.

Advantages	Limitations
Without air nor fuel pre-heating, achieving lean-premixed combustion with near zero NOx and CO emissions of the dual-fuel G/M 60/40-methane with the methane amount of 0–3.0 kW.	Approximation of the properties of combustion products as air properties, that leads to the qualitative estimate of the combustion completeness.
Determining the optimum methane amount to enhance the efficiency of the dual-fuel combustion of G/M 60/40-methane blends.	Use of unburned hydrocarbon measurement device can provide more accurate results of combustion completeness.
Achieving complete combustion of G/M 60/40-methane blends with a small amount of methane at 1 kW by using the novel SB injector at an ALR of 2.5, enabling use of waste crude glycerol as a biofuel.	Current simple flame color imaging could not provide more insight into the flame characteristics compared to other advanced optical diagnostics.

Future work will further investigate the reacting spray physics including the droplet size and velocity distribution and correlate with the downstream combustion characteristics to elucidate the fundamental physicochemical characteristics of the spray combustion using the SB injection.

Author Contributions: S.M.R.I.: experimentation, methodology, formal analysis, and writing—original draft and writing—review and editing. I.P.: experimentation, methodology, data curation, and writing–revising original draft. L.J.: conceptualization, methodology, resources, project administration, supervision, funding acquisition, formal analysis, and writing—review and editing. All authors have read and agreed to the published version of the manuscript.

Funding: The current research is funded by the Startup fund of Baylor University and NSF CIVIC award No. 2228311 and No. 2322319 co-funded by US National Science Foundation and Department of Energy.

Institutional Review Board Statement: Not applicable for this study.

Informed Consent Statement: Not applicable for this study

Data Availability Statement: Data will be made available on request.

Acknowledgments: We would also like to express our gratitude to Ashely Orr, who helped manufacture the combustion system and Joseph Breerwood for helping set up the system and Tony Bui for partial data collection. The paper is the extended version of the conference contribution here: https://arc.aiaa.org/doi/10.2514/6.2024-0331, (8 January 2024).

Conflicts of Interest: The authors declare that there are no competing financial interests nor personal relationships that could influence the work reported in this paper.

Nomenclature

AA	atomizing air or gas
AB	air blast
ALR	air or gas to liquid mass ratio
AO	algae oil
CH_4	methane
CO	carbon monoxide
D	diameter of the center liquid fuel channel and the injector exit
FB	flow blurring
G/M	glycerol/methanol
LPM	lean premixed combustion
H	gap between the center liquid fuel channel tip and injector exit
HRR	heat release rate
MFC	mass flow controller
MLPM	milliliter per minute
NG	natural gas
NOx	nitrogen oxides (including NO and NO_2)
PA	primary air
SB	swirl burst
SLPM	standard liter per minute
SMD	Sauter mean diameter
SN	swirl number
VO	vegetable oil
d_h	hub diameter
d_t	tip diameter
α	exit vane angle

References

1. Suhara, A.; Karyadi; Herawan, S.G.; Tirta, A.; Idris, M.; Roslan, M.F.; Putra, N.R.; Hananto, A.L.; Veza, I. Biodiesel Sustainability: Review of Progress and Challenges of Biodiesel as Sustainable Biofuel. *Clean Technol.* **2024**, *6*, 886–906. https://doi.org/10.3390/cleantechnol6030045.
2. Leung, D.Y.C.; Wu, X.; Leung, M.K.H. A Review on Biodiesel Production Using Catalyzed Transesterification. *Appl. Energy* **2010**, *87*, 1083–1095. https://doi.org/10.1016/j.apenergy.2009.10.006.
3. Farag, H.A.; El-Maghraby, A.; Taha, N.A. Transesterification of Esterified Mixed Oil for Biodiesel Production. *Int. J. Chem. Biochem. Sci.* **2012**, *2*, 105–114.
4. Yuan, Z.; Xia, S.; Chen, P.; Hou, Z.; Zheng, X. Etherification of Biodiesel-Based Glycerol with Bioethanol over Tungstophosphoric Acid To Synthesize Glyceryl Ethers. *Energy Fuels* **2011**, *25*, 3186–3191. https://doi.org/10.1021/ef200366q.
5. Quispe, C.A.G.; Coronado, C.J.R.; Carvalho, J.A., Jr. Glycerol: Production, Consumption, Prices, Characterization and New Trends in Combustion. *Renew. Sustain. Energy Rev.* **2013**, *27*, 475–493. https://doi.org/10.1016/j.rser.2013.06.017.
6. Feng, C.; Zhang, M.; Wu, H. Combustion of Fuel Mixtures Containing Crude Glycerol (CG): Important Role of Interactions between CG and Fuel Components in Particulate Matter Emission. *Ind. Eng. Chem. Res.* **2018**, *57*, 4132–4138. https://doi.org/10.1021/acs.iecr.8b00441.
7. Jiang, L.; Agrawal, A.K. Combustion of Straight Glycerol with/without Methane Using a Fuel-Flexible, Low-Emissions Burner. *Fuel* **2014**, *136*, 177–184. https://doi.org/10.1016/j.fuel.2014.07.027.
8. Islam, S.M.R.; Patel, I.; Jiang, L. Effect of Methane in Global Combustion Characteristics of Glycerol and Methanol Blend by Using a Novel Swirl Burst Injector. In Proceedings of the 2024 AIAA SciTech Forum and Exposition, Orlando, FL, USA, 8–12 January 2024.
9. He, Q.; McNutt, J.; Yang, J. Utilization of the Residual Glycerol from Biodiesel Production for Renewable Energy Generation. *Renew. Sustain. Energy Rev.* **2017**, *71*, 63–76. https://doi.org/10.1016/j.rser.2016.12.110.
10. Zhang, J.; Wang, Y.; Muldoon, V.L.; Deng, S. Crude Glycerol and Glycerol as Fuels and Fuel Additives in Combustion Applications. *Renew. Sustain. Energy Rev.* **2022**, *159*, 112206. https://doi.org/10.1016/j.rser.2022.112206.
11. Chilakamarry, C.R.; Mimi Sakinah, A.M.; Zularisam, A.W.; Pandey, A.; Vo, D.-V.N. Technological Perspectives for Utilisation of Waste Glycerol for the Production of Biofuels: A Review. *Environ. Technol. Innov.* **2021**, *24*, 101902. https://doi.org/10.1016/j.eti.2021.101902.
12. Agwu, O.; Valera-Medina, A.; Katrašnik, T.; Seljak, T. Flame Characteristics of Glycerol/Methanol Blends in a Swirl-Stabilised Gas Turbine Burner. *Fuel* **2021**, *290*, 119968. https://doi.org/10.1016/j.fuel.2020.119968.

13. Deka, T.J.; Osman, A.I.; Baruah, D.C.; Rooney, D.W. Methanol Fuel Production, Utilization, and Techno-Economy: A Review. *Environ. Chem. Lett.* **2022**, *20*, 3525–3554. https://doi.org/10.1007/s10311-022-01485-y.
14. Jiang, L.; Hall, T.; Williams, D.; Swinney, R. Global Combustion Characteristics of Glycerol and Methanol Blends Using a Novel Fuel-Flexible Injector. In Proceedings of the 2023 AIAA SCITECH Forum, Online, National Harbor, MD, USA, 23–27 January 2023.
15. Lefebvre, A.H. Airblast Atomization. *Prog. Energy Combust. Sci.* **1980**, *6*, 233–261. https://doi.org/10.1016/0360-1285(80)90017-9.
16. Simmons, B.M.; Agrawal, A.K. Spray Characteristics of a Flow-Blurring Atomizer. *At. Sprays* **2010**, *20*, 821–835. https://doi.org/10.1615/AtomizSpr.v20.i9.60.
17. Akinyemi, O.S.; Jiang, L. Development and Combustion Characterization of a Novel Twin-Fluid Fuel Injector in a Swirl-Stabilized Gas Turbine Burner Operating on Straight Vegetable Oil. *Exp. Therm. Fluid Sci.* **2019**, *102*, 279–290. https://doi.org/10.1016/j.expthermflusci.2018.11.014.
18. Institute of Mechanics and Thermodynamics, Chemnitz University of Technology, Chemnitz, Germany; Roudini, M.; Wozniak, G. Investigation of the Secondary Atomization in Prefilming Air-Blast Atomizers. *IJCEA* **2019**, *10*, 138–143. https://doi.org/10.18178/ijcea.2019.10.5.757.
19. Guildenbecher, D.R.; López-Rivera, C.; Sojka, P.E. Secondary Atomization. *Exp. Fluids* **2009**, *46*, 371–402. https://doi.org/10.1007/s00348-008-0593-2.
20. Bhayaraju, U.; Hassa, C. Planar Liquid Sheet Breakup of Prefilming and Nonprefilming Atomizers at Elevated Pressures. *At. Sprays* **2009**, *19*, 1147–1169. https://doi.org/10.1615/AtomizSpr.v19.i12.50.
21. Simmons, B.M.; Panchasara, H.V.; Agrawal, A.K. A Comparison of Air-Blast and Flow-Blurring Injectors Using Phase Doppler Particle Analyzer Technique. In Proceedings of the ASME Turbo Expo, Orlando, FL, USA, 8–12 June 2009; pp. 981–992.
22. Qavi, I.; Jiang, L.; Akinyemi, O.S. Near-Field Spray Characterization of a High-Viscosity Alternative Jet Fuel Blend C-3 Using a Flow Blurring Injector. *Fuel* **2021**, *293*, 120350. https://doi.org/10.1016/j.fuel.2021.120350.
23. Hendershott, T.H.; Stouffer, S.; Monfort, J.R.; Diemer, J.; Busby, K.; Corporan, E.; Wrzesinski, P.; Caswell, A.W. Ignition of Conventional and Alternative Fuel at Low Temperatures in a Single-Cup Swirl-Stabilized Combustor. In Proceedings of the AIAA Aerospace Sciences Meeting, Kissimmee, FL, USA, 8–12 January 2018.
24. Gañán-Calvo, A.M. Enhanced Liquid Atomization: From Flow-Focusing to Flow-Blurring. *Appl. Phys. Lett.* **2005**, *86*, 214101. https://doi.org/10.1063/1.1931057.
25. Panchasara, H.V.; Sequera, D.E.; Schreiber, W.C.; Agrawal, A.K. Emissions Reductions in Diesel and Kerosene Flames Using a Novel Fuel Injector. *J. Propuls. Power* **2009**, *25*, 984–987. https://doi.org/10.2514/1.37165.
26. Jiang, L.; Agrawal, A.K. Spray Features in the near Field of a Flow-Blurring Injector Investigated by High-Speed Visualization and Time-Resolved PIV. *Exp. Fluids* **2015**, *56*, 103. https://doi.org/10.1007/s00348-015-1973-z.
27. Simmons, B.M.; Agrawal, A.K. Drop Size and Velocity Measurements in Bio-Oil Sprays Produced by the Flow-Blurring Injector. In Proceedings of the ASME Turbo Expo, ASMEDC, Vancouver, BC, Canada, 6–10 June 2011; pp. 701–710.
28. Panchasara, H.V.; Simmons, B.M.; Agrawal, A.K.; Spear, S.K.; Daly, D.T. Combustion Performance of Biodiesel and Diesel-Vegetable Oil Blends in a Simulated Gas Turbine Burner. In Proceedings of the ASME Turbo Expo, Berlin, Germany, 9–13 June 2008.
29. Qavi, I.; Jiang, L. Optical Characterization of Near-Field Sprays for Various Alternative and Conventional Jet Fuels Using a Flow-Blurring Injector. *Flow Turbul. Combust.* **2022**, *108*, 599–624. https://doi.org/10.1007/s10494-021-00276-9.
30. Jiang, L.; Agrawal, A.K. Investigation of Glycerol Atomization in the Near-Field of a Flow-Blurring Injector Using Time-Resolved PIV and High-Speed Visualization. *Flow Turbul. Combust.* **2015**, *94*, 323–338. https://doi.org/10.1007/s10494-014-9572-2.
31. Simmons, B.M.; Agrawal, A.K. Flow Blurring Atomization for Low-Emission Combustion of Liquid Biofuels. *Combust. Sci. Technol.* **2012**, *184*, 660–675. https://doi.org/10.1080/00102202.2012.660222.
32. Sharma, S.; Biswal, Y.; Drabo, M.; Kolhe, P.S. Effect of Flow Field on Glycerol Combustion in a Swirl Stabilized Combustor Employing Flow Blurring Atomizer. In Proceedings of the 9th Thermal and Fluids Engineering Conference (TFEC), Corvallis, OR, USA, 21–24 April 2024.
33. Biswal, Y.; Sharma, S.; Warghat, K.V.; Nayak, G.M.; Drabo, M.; Kolhe, P.S. Characterization of Flame Morphology for Twin Fluid Atomizer-Based Swirl Stabilized Combustor. In Proceedings of the AIAA SCITECH Forum, Orlando, FL, USA, 8–12 January 2024.
34. Jiang, L.; Akinyemi, O.S.; Danh, V. Investigation of Combustion Characteristics of Straight Vegetable Oil for a Novel Twin-Fluid Fuel Injector: Heterogeneous Combustion. In Proceedings of the 10th U. S. National Combustion Meeting Organized by the Eastern States Section of the Combustion Institute, College Park, MD, USA, 23–26 April 2017.
35. Danh, V.; Akinyemi, O.S.; Taylor, C.E.; Frank, J.T.; Jiang, L. Effect of Injector Swirl Number on Near-Field Spray Characteristics of a Novel Twin-Fluid Injector. *Exp. Fluids* **2019**, *60*, 80. https://doi.org/10.1007/s00348-019-2721-6.
36. Akinyemi, O.S.; Jiang, L.; Hernandez, R.; McIntyre, C.; Holmes, W. Combustion of Straight Algae Oil in a Swirl-Stabilized Burner Using a Novel Twin-Fluid Injector. *Fuel* **2019**, *241*, 176–187. https://doi.org/10.1016/j.fuel.2018.12.006.
37. Akinyemi, O.S.; Qavi, I.; Taylor, C.E.; Jiang, L. Effect of the Air-to-Liquid Mass Ratio on the Internal Flow and near-Field Spray Characteristics of a Two-Phase Swirl Burst Injector. *J. Aerosol Sci.* **2023**, *167*, 106092. https://doi.org/10.1016/j.jaerosci.2022.106092.
38. Breerwood, J.; Jiang, L.; Ahmed, M.S. Near-Field Spray Characteristics and Steadiness of a Novel Twin-Fluid Injector with Enhanced Primary Atomization. *J. Aerosol Sci.* **2024**, *180*, 106402. https://doi.org/10.1016/j.jaerosci.2024.106402.

39. Ahmed, M.S.; Cary, J.; Fezzaa, K.; Clark, S.; McClain, S.T.; Jiang, L. Effect of Internal and External Swirls on Near-Field Spray Characteristics of Swirl Burst Injectors Using High-Speed X-Ray Imaging. In Proceedings of the AIAA SCITECH Forum, Orlando, FL, USA, 8–12 January 2024.
40. Danh, V.; Jiang, L.; Akinyemi, O.S. Investigation of Water Spray Characteristics in the near Field of a Novel Swirl Burst Injector. *Exp. Therm. Fluid Sci.* **2019**, *102*, 376–386. https://doi.org/10.1016/j.expthermflusci.2018.12.014.
41. Murugan, R.; Kolhe, P.S.; Sahu, K.C. A Combined Experimental and Computational Study of Flow-Blurring Atomization in a Twin-Fluid Atomizer. *Eur. J. Mech.—B/Fluids* **2020**, *84*, 528–541. https://doi.org/10.1016/j.euromechflu.2020.07.008.
42. Ling, Y.; Jiang, L. A Detailed Numerical Investigation of Two-Phase Flows Inside a Planar Flow-Blurring Atomizer. *At. Sprays* **2024**, *34*, 1–20. https://doi.org/10.1615/AtomizSpr.2023049089.
43. Nasim, M.N.; Qavi, I.; Jiang, L. Effect of Varying Internal Geometry on the Near-Field Spray Characteristics of a Swirl Burst Injector. *Flow Turbul. Combust.* **2023**, *111*, 641–674. https://doi.org/10.1007/s10494-023-00441-2.
44. Cravero, C.; Marogna, N.; Marsano, D. A Numerical Study of Correlation Between Recirculation Length and Shedding Frequency in Vortex Shedding Phenomena. *WSEAS Trans. Fluid Mech.* **2021**, *16*, 48–62. https://doi.org/10.37394/232013.2021.16.6.
45. Shi, L.; Yang, G.; Yao, S. Large Eddy Simulation of Flow Past a Square Cylinder with Rounded Leading Corners: A Comparison of 2D and 3D Approaches. *J. Mech. Sci. Technol.* **2018**, *32*, 2671–2680. https://doi.org/10.1007/s12206-018-0524-y.
46. Papagiannakis, R.G.; Hountalas, D.T. Combustion and Exhaust Emission Characteristics of a Dual Fuel Compression Ignition Engine Operated with Pilot Diesel Fuel and Natural Gas. *Energy Convers. Manag.* **2004**, *45*, 2971–2987. https://doi.org/10.1016/j.enconman.2004.01.013.
47. Guido, C.; Alfè, M.; Gargiulo, V.; Napolitano, P.; Beatrice, C.; Del Giacomo, N. Chemical/Physical Features of Particles Emitted from a Modern Automotive Dual-Fuel Methane–Diesel Engine. *Energy Fuels* **2018**, *32*, 10154–10162. https://doi.org/10.1021/acs.energyfuels.8b01011.
48. Malaquias, A.C.T.; da Costa, R.B.R.; Netto, N.A.D.; Coronado, C.J.R.; Baêta, J.G.C. A Review of Dual-Fuel Combustion Mode in Spark-Ignition Engines. *J. Braz. Soc. Mech. Sci. Eng.* **2021**, *43*, 426. https://doi.org/10.1007/s40430-021-03156-5.
49. Di Iorio, S.; Sementa, P.; Vaglieco, B.M. Experimental Investigation of a Methane-Gasoline Dual-Fuel Combustion in a Small Displacement Optical Engine. In Proceedings of the 11th International Conference on Engines & Vehicles, Capri, Napoli, Italy, 15–19 September 2013.
50. Altaher, M.A.; Li, H.; Andrews, G.E. Co-Firing of Kerosene and Biodiesel With Natural Gas in a Low NOx Radial Swirl Combustor. In *Volume 1: Aircraft Engine; Ceramics; Coal, Biomass and Alternative Fuels; Controls, Diagnostics and Instrumentation, Proceedings of the ASME Turbo Expo 2012, Copenhagen, Denmark, 11–15 June 2012*; American Society of Mechanical Engineers: New York, NY, USA, 2012; pp. 557–567.
51. Chong, C.T.; Chiong, M.-C.; Ng, J.-H.; Tran, M.-V.; Valera-Medina, A.; Józsa, V.; Tian, B. Dual-Fuel Operation of Biodiesel and Natural Gas in a Model Gas Turbine Combustor. *Energy Fuels* **2020**, *34*, 3788–3796. https://doi.org/10.1021/acs.energyfuels.9b04371.
52. Hall, T.; Williams, D.; Islam, S.M.R.; Patel, I.; Chakmakjian, C.; Jiang, L. Clean Co-Combustion of Glycerol and Methanol Blends Using a Novel Fuel-Flexible Injector. *Fuel* **2024**, *371*, 132125. https://doi.org/10.1016/j.fuel.2024.132125.
53. Lilley, D.G. Swirl Flows in Combustion: A Review. *AIAA J.* **1977**, *15*, 1063–1078. https://doi.org/10.2514/3.60756.
54. Khandelwal, B.; Lili, D.; Sethi, V. Design and Study on Performance of Axial Swirler for Annular Combustor by Changing Different Design Parameters. *J. Energy Inst.* **2014**, *87*, 372–382. https://doi.org/10.1016/j.joei.2014.03.022.
55. Li, Z.; Wang, Y.; Geng, H.; Zhen, X.; Liu, M.; Xu, S.; Li, C. Effects of Diesel and Methanol Injection Timing on Combustion, Performance, and Emissions of a Diesel Engine Fueled with Directly Injected Methanol and Pilot Diesel. *Appl. Therm. Eng.* **2019**, *163*, 114234. https://doi.org/10.1016/j.applthermaleng.2019.114234.
56. Wang, Y.; Wang, H.; Meng, X.; Tian, J.; Wang, Y.; Long, W.; Li, S. Combustion Characteristics of High Pressure Direct-Injected Methanol Ignited by Diesel in a Constant Volume Combustion Chamber. *Fuel* **2019**, *254*, 115598. https://doi.org/10.1016/j.fuel.2019.06.006.
57. Duraisamy, G.; Rangasamy, M.; Govindan, N. A Comparative Study on Methanol/Diesel and Methanol/PODE Dual Fuel RCCI Combustion in an Automotive Diesel Engine. *Renew. Energy* **2020**, *145*, 542–556. https://doi.org/10.1016/j.renene.2019.06.044.
58. Seljak, T.; Katrašnik, T. Emission Reduction through Highly Oxygenated Viscous Biofuels: Use of Glycerol in a Micro Gas Turbine. *Energy* **2019**, *169*, 1000–1011. https://doi.org/10.1016/j.energy.2018.12.095.
59. Ferreira, A.G.M.; Egas, A.P.V.; Fonseca, I.M.A.; Costa, A.C.; Abreu, D.C.; Lobo, L.Q. The Viscosity of Glycerol. *J. Chem. Thermodyn.* **2017**, *113*, 162–182. https://doi.org/10.1016/j.jct.2017.05.042.
60. Exclusively Canon, Essential for EOS Users. Available online: https://www.eos-magazine.com/articles/eospedia/what-is/iso.html (accessed on 12 October 2024).
61. Turns, S.R. *An Introduction to Combustion: Concepts and Applications*, 3rd ed.; McGraw-Hill: New York, NY, USA, 2012; ISBN 978-0-07-338019-3.
62. Li, S.; Qian, W.; Liu, H.; Liu, G.; Zhu, M. Autoignition and Flame Lift-off Behavior of a Fuel Jet Mixing with Turbulent Hot Air Coflow. *Proc. Combust. Inst.* **2021**, *38*, 6385–6392. https://doi.org/10.1016/j.proci.2020.06.230.
63. Kalghatgi, T.G. Lift-off Heights and Visible Lengths of Vertical Turbulent Jet Diffusion Flames in Still Air. *Combust. Sci. Technol.* **1984**, *41*, 17–29. https://doi.org/10.1080/00102208408923819.
64. Çengel, Y.A.; Ghajar, A.J. *Heat and Mass Transfer: Fundamentals & Applications*, 5th ed.; McGraw Hill Education: New York, NY, USA, 2015; ISBN 978-0-07-339818-1.

65. Bradley, D.; Entwistle, A.G. Determination of the Emissivity, for Total Radiation, of Small Diameter Platinum-10% Rhodium Wires in the Temperature Range 600-1450 C. *Br. J. Appl. Phys.* **1961**, *12*, 708–711. https://doi.org/10.1088/0508-3443/12/12/328.
66. Hindasageri, V.; Vedula, R.P.; Prabhu, S.V. Thermocouple Error Correction for Measuring the Flame Temperature with Determination of Emissivity and Heat Transfer Coefficient. *Rev. Sci. Instrum.* **2013**, *84*, 024902. https://doi.org/10.1063/1.4790471.
67. Yan, W.; Panahi, A.; Levendis, Y.A. Spectral Emissivity and Temperature of Heated Surfaces Based on Spectrometry and Digital Thermal Imaging—Validation with Thermocouple Temperature Measurements. *Exp. Therm. Fluid Sci.* **2020**, *112*, 110017. https://doi.org/10.1016/j.expthermflusci.2019.110017.
68. Petrov, V.; Reznik, V. Measurement of the Emissivity of Quartz Glass. *High Temp.-High Press.* **1972**, *4*, 687–693.
69. Çengel, Y.A. *Heat Transfer: A Practical Approach*, 2nd ed.; McGraw-Hill Companies: New York, NY, USA, 2002; ISBN 0-07-245893-3.
70. Shannon, K.S.; Butler, B.W. A Review of Error Associated with Thermocouple Temperature Measurement in Fire Environments. In Proceedings of the 2nd International Wildland Fire Ecology and Fire Management Congress and the 5th Symposium on Fire and Forest Meteorology, Orlando, FL, USA, 16–20 November 2003.